THE JOURNAL OF PHYSICAL CHEMISTRY Letters

pubs.acs.org/JPCL Letter

# Femtosecond Transient Absorption Spectra and Dynamics of Carrier Relaxation of Tin Perovskites in the Absence and Presence of Additives

Sudhakar Narra, Efat Jokar, Orion Pearce, Chia-Yi Lin, Amir Fathi, and Eric Wei-Guang Diau*

Cite This: J. Phys. Chem. Lett. 2020, 11, 5699−5704 Read Online

ACCESS | Metrics & More | Article Recommendations | Supporting Information

**ABSTRACT:** The effects of additives $SnF_2$ (10%) and $EDAI_2$ (1%) on the dynamics of carrier relaxation of formamidinium tin triiodide ($FASnI_3$) perovskite were studied using femtosecond transient absorption spectra (TAS) with excitation at 600 and 870 nm. The TAS were analyzed according to a parallel sequential kinetic model with a global fit through singular-value decomposition. For excitation at 600 nm, two relaxation paths were found: one involved hot and cold carriers in the bulk state undergoing shallow bulk-defect-mediated charge recombination; the other involved trap carriers in the surface state undergoing deep surface-defect-mediated charge recombination. For excitation at 870 nm, only cold carriers were subjected to the bulk-state relaxation channel. Our spectral results indicate significant effects of the additives on retarding charge recombination in both bulk and surface states as well as decreasing the bandgap renormalization energy, the bandwidth of the photobleaching (PB) band, and the Stokes shift between the PB and photoluminescence bands, explaining how the device performance of $FASnI_3$ solar cells became enhanced in the presence of $SnF_2$ and $EDAI_2$.

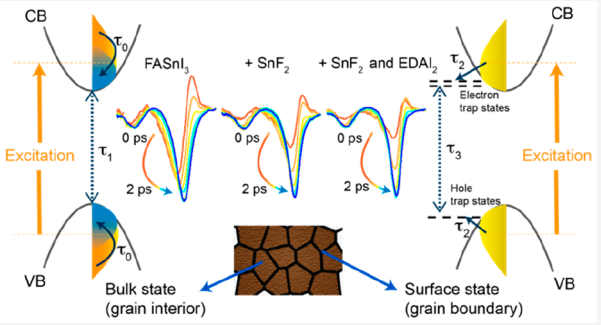


Tin-based (Sn) perovskites are at the forefront of research on perovskite solar cells (PSCs) as prospective candidates to replace toxic lead-based (Pb) PSCs.[1−4] Compared to Pb perovskites, Sn perovskites possess desirable properties for the efficiency of PSC that include a narrower bandgap, a smaller exciton binding energy,[5,6] a smaller carrier reduced mass,[7,8] and a greater mobility,[5,9,10] but these advantages have not yet been reflected in their device performances. The poor performance of Sn PSCs has been attributed to their large background carrier density of holes caused by oxidation of $Sn^{2+}$ to $Sn^{4+}$, leading to a blue shift of the absorption onset, decreased mobility, and rapid relaxation of photoexcited carriers to the ground state.[5,11] Recent attempts to enhance the efficiency of Sn PSC have been directed to suppress the background hole density and to improve the Sn perovskite morphologies through addition of $SnF_2$ and co-additives such as ethylenediammonium diiodide ($EDAI_2$),[12−14] phenylethylammonium iodide (PEAI),[15] PEABr,[16] PEACl,[17] $NH_3SCN$,[18] $GeI_2$,[19] and others.[3,4]

For Sn PSCs, experiments[5,20] showed that background carrier densities are affected by growth conditions whereas theoretical calculations[21−25] indicated small energies of formation of $Sn^{2+}$ vacancies. An enhanced understanding of the defect-induced charge recombination dynamics of Sn perovskites under various growth conditions is hence crucial for improving the performance of Sn-based PSC devices. Time-resolved spectral techniques in the terahertz region,[5] fluorescence decay,[6,8,9,19,26−30] and transient absorption spectra (TAS)[15,31] were employed to probe the dynamics of carrier recombination and mechanisms of carrier cooling in Sn perovskites, but a detailed assessment of the influence of additives on the type of defects and their role in recombination rates has not yet been reported. To enhance the performance of a $FASnI_3$ device, we showed[12,13] that co-additive $EDAI_2$ and additive $SnF_2$ are required to control the film morphology, to passivate the surface defect states, and to relax the crystal strain. In the work presented here, we performed femtosecond TAS experiments on three samples [$FASnI_3$, $FASnI_3$ with 10% $SnF_2$, and $FASnI_3$ with 10% $SnF_2$ and 1% $EDAI_2$ (to which we refer as pristine, $SnF_2$, and $EDAI_2$, respectively)] to identify the spectral signatures of defect states and the role of $SnF_2$ and $EDAI_2$ in carrier recombination paths. Our TAS results indicated defects of two types, namely, bulk (shallow) and surface (deep) defects, which became suppressed with additives in Sn perovskites. This finding has enabled us to reveal the significance of these additives in decreasing the effect of defect states, and thereby to retard the recombination of

Received: May 22, 2020
Accepted: July 1, 2020
Published: July 1, 2020







https://dx.doi.org/10.1021/acs.jpclett.0c01589
J. Phys. Chem. Lett. 2020, 11, 5699−5704

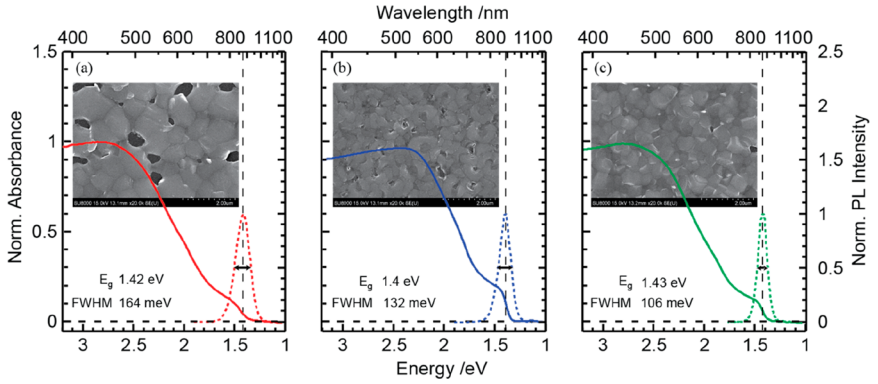


**Figure 1.** Absorption spectra, photoluminescence (PL) spectra, and SEM images of (a) pristine, (b) $SnF_2$, and (c) $EDAI_2$ samples. The bandgap ($E_g$) is determined by the maximum of the PL feature; the corresponding bandwidths (full widths at half-maximum) of the PL bands are shown for each sample.

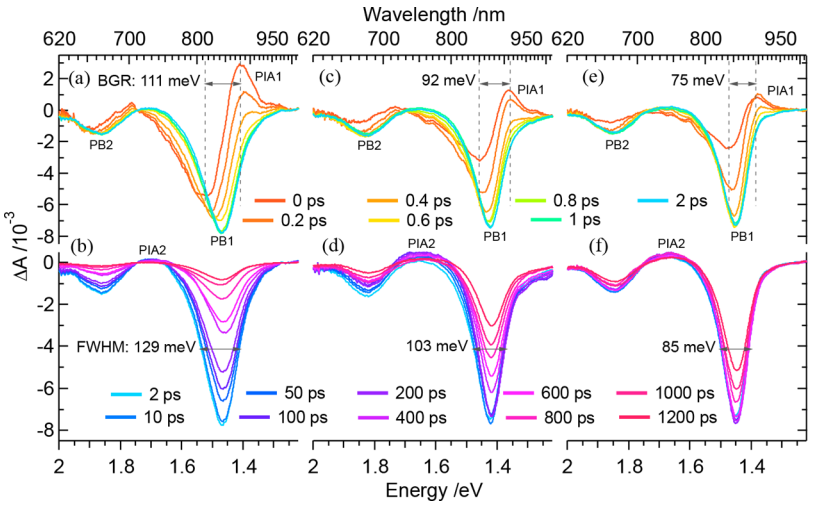


**Figure 2.** Transient absorption spectra (TAS) of (a and b) pristine, (c and d) $SnF_2$, and (e and f) $EDAI_2$ samples probed at varied delays as indicated. The samples were excited with a laser pulse at 600 nm (2.07 eV) with a fluence of 1.4 $\mu$J cm$^{-2}$. The spectra of pristine and $SnF_2$ are scaled to the spectral intensity of $EDAI_2$ for the sake of clarity.

carrier charges and to improve the performance of Sn-based PSCs.

Samples of $FASnI_3$ perovskites as thin films in the pristine, $SnF_2$, and $EDAI_2$ forms were spin-coated on glass substrates as reported elsewhere.[12] The crystallinity and morphology of the samples were characterized by X-ray diffraction (XRD) and a scanning electron microscope (SEM), respectively. The XRD patterns (Figure S1) confirm the formation of perovskite films with a slightly increased volume of the unit cell (Table S1), whereas the SEM images (insets in Figure 1) reflect the quality of film formation improved with additives. After confirming the formation of perovskite films, we studied the effects of additives on their optical properties based on steady-state absorption and photoluminescence (PL) spectra; the results are shown in Figure 1. The absorption spectra of the three perovskite samples show a broad continuum with a bandgap transition near 1.4 eV. The maxima of the PL features determine the bandgaps ($E_g$), which are 1.41, 1.40, and 1.43 eV for the pristine, $SnF_2$, and $EDAI_2$ samples, respectively. The corresponding PL bandwidths tend to decrease from 164 meV (pristine) to 132 meV ($SnF_2$) to 104 meV ($EDAI_2$), through the suppression of defects caused by oxidation of $Sn^{2+}$ to $Sn^{4+}$ in the presence of additive $SnF_2$ and co-additive $EDAI_2$, which is confirmed by X-ray photoelectron spectra (XPS) shown in Figure S2 and Table S2.

Femtosecond TAS experiments with excitation at 600 nm and a probe in the region of 620−1010 nm produced the defect-associated spectra and kinetics of these three samples. TAS of pristine, $SnF_2$, and $EDAI_2$ samples measured in subpicosecond (panels a, c, and e) and picosecond to nanosecond (panels b, d, and f) regions are shown in Figure 2. All perovskite samples showed transient spectral features similar to those observed for other Pb[32−35] and Sn perovskites;[15,31] the assignments were made accordingly. First, the strong photobleached band (PB) in the long-wavelength region is assigned as PB1 whereas the weak one in the short-wavelength region is assigned as PB2. Second, the sub-bandgap photoinduced absorption (PIA) is assigned as PIA1; the faint high-energy PIA between PB1 and PB2 is assigned as PIA2. In general, the subpicosecond TAS (Figure 2a,c,e) show red-shifted progressions of both bands PB1 and PB2 with a rapid decay of band PIA1. In contrast, the picosecond to nanosecond TAS (Figure 2b,d,f) show slow recoveries of both bands PB1 and PB2 with a small change for band PIA2.

On the basis of the similarity of TA spectral bands with Pb perovskites,[33] the origins of the PB1 and PB2 bands observed here are assigned to transitions between valence band 1 (VB1)


https://dx.doi.org/10.1021/acs.jpclett.0c01589
J. Phys. Chem. Lett. 2020, 11, 5699−5704

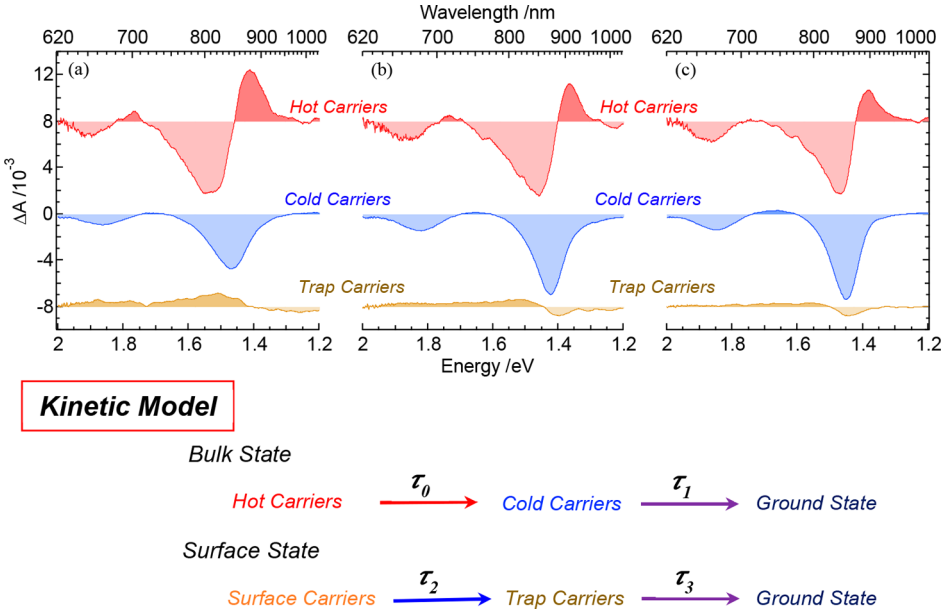


**Figure 3.** SVD-deconvoluted component spectra of (a) pristine, (b) $SnF_2$, and (c) $EDAI_2$ samples and the kinetic model used for the deconvolution.

and conduction band 1 (CB1) (low energy) and between VB2 and CB1 (high energy); the early shifts in bands PB1 and PB2 were attributed to renormalization of the bandgap following excitation above that bandgap.[32,34,35] We similarly attribute broadening on the high-energy side of band PB1 and the rapid decay of band PIA1 to the presence of hot carriers undergoing subsequent cooling and PIA2 to the change in the refractive index due to photoexcitation.[32,34,36] As shown in panels a, c, and e of Figure 2, both bandgap renormalization and hot carrier cooling occur within ∼1 ps for all samples after photoexcitation. Bandgap renormalization occurs due to Coulomb corrections of VB and CB caused by photoinduced hot carriers. The magnitude of bandgap renormalization, termed a bandgap renormalization energy (BGR) shown in Figure 2, is estimated empirically from the difference in the energies of the PB1 minimum and PIA1 maximum at time zero before band filling occurred, as this difference expresses the extent of the change in the bandgap immediately after photoexcitation.[35] The TAS of the pristine sample exhibited renormalization that was larger than those of samples containing $SnF_2$ and $EDAI_2$ additives. The estimated BGR are 111, 92, and 75 meV for pristine, $SnF_2$, and $EDAI_2$ samples, respectively. Band PB1 at the minimum (∼2 ps) of the pristine sample showed a Stokes shift 50 meV from the bandgap estimated from the PL maximum, whereas the $SnF_2$ and $EDAI_2$ samples showed shifts of ∼20 and ∼10 meV, respectively. The additives caused narrowing of band PB1; the corresponding full width at half-maximum (fwhm) values are 129, 103, and 85 meV for pristine, $SnF_2$, and $EDAI_2$ samples, respectively (Figure 2). The decreased BGR, Stokes shift, and fwhm indicate a suppression of the background carrier population, as unpaired carriers lead to a decreased oscillator strength of the bandgap through Coulomb blocking.[34] Our observations thus indicate that added $SnF_2$ and $EDAI_2$ play complementary roles in removing defect states and decreasing the concentration of background carriers to improve the device performance for tin perovskites.

Band PIA1 observed in the sub-bandgap region with ultrafast decay is similar to the feature observed in the TAS of $MAPbI_3$ due to the absorption of the hot carriers.[34] As a result, we recorded TAS of pristine, $SnF_2$, and $EDAI_2$ samples at near-bandgap excitation (1.425 eV or 870 nm); the results are shown in Figure S3. The TAS in Figure S3 (panels a, c, and e) show no contribution of band PIA1, asymmetric band broadening to the blue side, or renormalization of the PB1 band after photoexcitation, indicating that resonant excitation solely produces cold carriers. Instead, both PB bands show recombination in the picosecond to nanosecond region similar to the case of above-bandgap excitation.

Analysis of the corresponding transient profiles of the TAS shown in Figure 2 is complicated because they contain many components to be resolved. To solve this problem, we applied a global fitting procedure using singular-value decomposition (SVD).[37,38] The details of the SVD analysis are described in the Supporting Information. Briefly, SVD was used to extract the kinetic and spectral components based on a suitable kinetic model. A consecutive kinetic model was first applied, judging from the rapid decay of band PIA1 (hot carriers) as well as the rapid evolution (cold carriers) and slow recovery (charge recombination) of both bands PB1 and PB2, but the transient profiles were poorly fitted with a single sequential kinetic model. As a result, we introduced a second consecutive process involving an additional intermediate (trap carriers) in a parallel kinetic model shown in Figure 3. After the global fitting, three observable components representing hot carriers, cold carriers, and trap carriers are shown in Figure 3. We assign the two sequential kinetic processes to occur in the bulk (grain interior) and surface (grain boundary) states, respectively. The associated decay coefficients, $\tau_0$ and $\tau_1$, hence represent the cooling of hot carriers and defect-associated charge recombination in the bulk state, respectively; $\tau_2$ and $\tau_3$ represent the formation of trap carriers and defect-associated charge recombination in the surface state, respectively. The fitted decay coefficients and the related carrier relaxation mechanism


https://dx.doi.org/10.1021/acs.jpclett.0c01589
J. Phys. Chem. Lett. 2020, 11, 5699−5704

are shown in Figure 4. A discussion of these kinetic results follows.

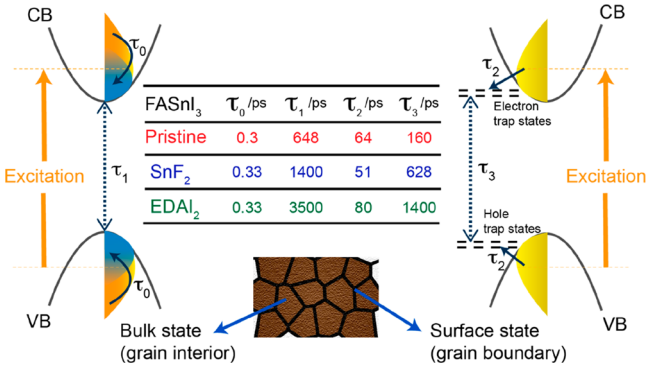


**Figure 4.** Mechanism of carrier relaxation for excitation above the bandgap from the bulk state and the surface state. The fitted decay coefficients of pristine, $SnF_2$, and $EDAI_2$ samples are listed in the table.

Excitation at 600 nm generated hot carriers in both bulk and surface states. Cooling of hot carriers in the bulk state took ~0.3 ps ($\tau_1$) for all three samples, but cooling in the surface state was not observed. The cooling of the hot surface carriers might be too rapid to be observed, because the TA imaging result showed that cooling is more rapid for hot carriers at grain boundaries than for those in the grain interiors in lead perovskites.[39] The fact that cold surface carriers were not detectable in our system might be due to the small portion of the carriers generated at the grain boundaries. We observed the formation of trap carriers in 50−80 ps ($\tau_3$) in the surface state for the three samples, but this component (trap carrier) was not observed upon excitation at 870 nm (Figure S3). Excitation above the bandgap involves dissipation of the excess energy of hot carriers to the lattice, which thereby supplies the necessary activation energy for the surface carriers moving to the surface trap state.[40] Excitation above the bandgap can thus populate both shallow bulk defects and deep surface defects, whereas excitation near the bandgap can populate only shallow bulk defects because excess energy is not available to activate the deep surface defects. The deep surface defects discussed here are high-lying defects in the valence and conduction bands and should not be confused with midbandgap states that are present in the middle of the VB and CB bands and cannot be observed with our probe in the visible and near-infrared region.

For the relaxation mechanism shown in Figure 4, the decay coefficients for the defect-assisted charge recombination are represented as $\tau_1$ in the bulk state and $\tau_3$ in the surface state. We observed a systematic trend that both $\tau_1$ and $\tau_3$ increased from the pristine to the $SnF_2$ to the $EDAI_2$ samples, indicating that both bulk and surface defects can be effectively suppressed in the presence of $SnF_2$ or $SnF_2$ and $EDAI_2$. Comparison for each sample indicates a duration of charge recombination much shorter for trap carriers ($\tau_3$) than for bulk carriers ($\tau_1$), which is consistent with our assignment for the former and the latter to deep and shallow defects, respectively. The charge recombination is more retarded for the deep trap defects than for the shallow bulk defects in the presence of an additive and a co-additive; i.e., $\tau_1$ increased from 648 ps (pristine) to 3500 ps ($EDAI_2$), whereas $\tau_3$ increased from 160 ps (pristine) to 1400 ps ($EDAI_2$). The former increased 5-fold, whereas the latter increased 9-fold.

On the basis of quantum-chemical calculations on Sn perovskites,[41] Sn vacancies ($Sn_v$) are responsible for bulk (shallow) defects whereas interstitials of formamidinium ions ($FA_i$) are responsible for surface (deep) defects. Both $Sn_v$ and $FA_i$ have small formation energies,[41] whereas the deep defects have greater formation energy in the case of Pb perovskites,[22] which is a marked difference between Pb and Sn perovskites. In our case, passivating $FASnI_3$ with $SnF_2$ (10%) suppressed $FA_i$ on the surface ($\tau_1$; 160 ps vs 628 ps) more than $Sn_v$ in the bulk ($\tau_3$; 648 ps vs 1400 ps); further addition of $EDAI_2$ (1%) to a Sn-rich film suppressed both $FA_i$ and $Sn_v$ defects further as the rate of charge recombination of the $EDAI_2$ sample became lower than that of the $SnF_2$ sample in both relaxation paths. The passivation effects of additives are clearly manifested in terms of enhanced periods of both bulk- and surface-defect-mediated recombination explicable from the kinetics shown in Figure 4. Our TAS thus indicate that addition of $SnF_2$ and $EDAI_2$ to the $FASnI_3$ perovskite can efficiently decrease the number of both bulk and surface defects to retard the corresponding charge recombination for device performance enhanced as reported elsewhere.[12]

The ultrafast carrier relaxation dynamics of three tin perovskite $FASnI_3$ samples, pristine, $SnF_2$, and $EDAI_2$, were investigated using femtosecond transient absorption spectra (TAS). For excitation at 870 nm, only cold carriers were observed, but for excitation at 600 nm above the bandgap, hot, cold, and trapped carriers were observed. Two carrier relaxation paths, representing the carrier relaxation in the bulk (grain interior) and surface (grain boundary) states, were deduced according to a parallel sequential kinetic model for a global fit of the TAS data in the case of excitation above the bandgap. The cooling of hot carriers in the bulk state occurs within ~0.3 ps for all samples; the subsequent relaxations of the cold carriers mediated by the shallow bulk defects show a systematic trend with the decay coefficients decreasing in the following order: 3500 ps ($EDAI_2$) > 1400 ps ($SnF_2$) > 648 ps (pristine). The formation of surface trap carriers, which requires an activation energy, occurs in 50−80 ps; the subsequent relaxations of trap carriers mediated by deep surface defects also show a systematic trend with the decay coefficients decreasing in the following order: 1400 ps ($EDAI_2$) > 628 ps ($SnF_2$) > 160 ps (pristine). The observed trend of the kinetics of carrier relaxation is consistent with the decreasing trend of the bandgap renormalization energy, the spectral width of band PB1, and the Stokes shift between bands PB1 and PL in the presence of an additive and a co-additive. Our TAS results thus indicate that addition of $SnF_2$ (10%) and $EDAI_2$ (1%) significantly decreases the concentrations of shallow defects in the bulk state and the deep defects in the surface state so as to enhance the device performance as observed previously.[12]

## ■ ASSOCIATED CONTENT

### Supporting Information

The Supporting Information is available free of charge at https://pubs.acs.org/doi/10.1021/acs.jpclett.0c01589.

Additional observations (PDF)



https://dx.doi.org/10.1021/acs.jpclett.0c01589
J. Phys. Chem. Lett. 2020, 11, 5699−5704

## AUTHOR INFORMATION


### Corresponding Author

**Eric Wei-Guang Diau** − *Department of Applied Chemistry and Institute of Molecular Science and Center for Emergent Functional Matter Science, National Chiao Tung University, Hsinchu 30010, Taiwan;* orcid.org/0000-0001-6113-5679; Email: diau@mail.nctu.edu.tw

### Authors

**Sudhakar Narra** − *Department of Applied Chemistry and Institute of Molecular Science, National Chiao Tung University, Hsinchu 30010, Taiwan*

**Efat Jokar** − *Department of Applied Chemistry and Institute of Molecular Science and Center for Emergent Functional Matter Science, National Chiao Tung University, Hsinchu 30010, Taiwan*

**Orion Pearce** − *Department of Applied Chemistry and Institute of Molecular Science, National Chiao Tung University, Hsinchu 30010, Taiwan;* orcid.org/0000-0002-6240-3118

**Chia-Yi Lin** − *Department of Applied Chemistry and Institute of Molecular Science, National Chiao Tung University, Hsinchu 30010, Taiwan*

**Amir Fathi** − *Department of Applied Chemistry and Institute of Molecular Science, National Chiao Tung University, Hsinchu 30010, Taiwan;* orcid.org/0000-0002-2528-8405

Complete contact information is available at: https://pubs.acs.org/10.1021/acs.jpclett.0c01589


### Notes

The authors declare no competing financial interest.

## ACKNOWLEDGMENTS

The Taiwan Ministry of Science and Technology (MOST 108-2119-M-009-004) and the Center for Emergent Functional Matter Science of National Chiao Tung University from The Featured Areas Research Center Program within the framework of the Higher Education SPROUT Project by Taiwan Ministry of Education provided financial support. The authors thank the National Synchrotron Radiation Research Center (NSRRC), Taiwan, for providing us beamline time for our X-ray photoelectron spectroscopy experiments.

## REFERENCES


(1) Ke, W.; Stoumpos, C. C.; Kanatzidis, M. G. Unleaded" Perovskites: Status Quo and Future Prospects of Tin-Based Perovskite Solar Cells. *Adv. Mater.* **2019**, *31*, 1803230.

(2) Yang, W.; Igbari, F.; Lou, Y.; Wang, Z.; Liao, L. Tin Halide Perovskites: Progress and Challenges. *Adv. Energy Mater.* **2020**, *10*, 1902584.

(3) Diau, E. W.-G.; Jokar, E.; Rameez, M. Strategies to Improve Performance and Stability for Tin-Based Perovskite Solar Cells. *ACS. Energy Lett.* **2019**, *4*, 1930−1937.

(4) Gu, F.; Zhao, Z.; Wang, C.; Rao, H.; Zhao, B.; Liu, Z.; Bian, Z.; Huang, C. Lead-Free Tin-Based Perovskite Solar Cells: Strategies Toward High Performance. *Sol. RRL* **2019**, *3*, 1900213.

(5) Milot, R. L.; Klug, M. T.; Davies, C. L.; Wang, Z.; Kraus, H.; Snaith, H. J.; Johnston, M. B.; Herz, L. M. The Effects of Doping Density and Temperature on the Optoelectronic Properties of Formamidinium Tin Triiodide Thin Films. *Adv. Mater.* **2018**, *30*, 1804506.

(6) Zhang, H.; Liao, Q.; Wu, Y.; Zhang, Z.; Gao, Q.; Liu, P.; Li, M.; Yao, J.; Fu, H. 2D Ruddlesden−Popper Perovskites Microring Laser Array. *Adv. Mater.* **2018**, *30*, 1706186.

(7) Feng, J.; Xiao, B. Effective Masses and Electronic and Optical Properties of Nontoxic $MASnX_3$ (X = Cl, Br, and I) Perovskite Structures as Solar Cell Absorber: A Theoretical Study Using HSE06. *J. Phys. Chem. C* **2014**, *118*, 19655−19660.

(8) Fang, H.-H.; Adjokatse, S.; Shao, S.; Even, J.; Loi, M. A. Long-Lived Hot-Carrier Light Emission and Large Blue Shift in Formamidinium Tin Triiodide Perovskites. *Nat. Commun.* **2018**, *9*, 151.

(9) Milot, R. L.; Eperon, G. E.; Green, T.; Snaith, H. J.; Johnston, M. B.; Herz, L. M. Radiative Monomolecular Recombination Boosts Amplified Spontaneous Emission in $HC(NH_2)_2SnI_3$ Perovskite Films. *J. Phys. Chem. Lett.* **2016**, *7*, 4178−4184.

(10) Herz, L. M. Charge-Carrier Mobilities in Metal Halide Perovskites: Fundamental Mechanisms and Limits. *ACS Energy Lett.* **2017**, *2*, 1539−1548.

(11) Noel, N. K.; Stranks, S. D.; Abate, A.; Wehrenfennig, C.; Guarnera, S.; Haghighirad, A.-A.; Sadhanala, A.; Eperon, G. E.; Pathak, S. K.; Johnston, M. B.; Petrozza, A.; Herz, L. M.; Snaith, H. J. Lead-Free Organic−Inorganic Tin Halide Perovskites for Photovoltaic Applications. *Energy Environ. Sci.* **2014**, *7*, 3061−3068.

(12) Jokar, E.; Chien, C.-H.; Fathi, A.; Rameez, M.; Chang, Y.-H.; Diau, E. W.-G. Slow Surface Passivation and Crystal Relaxation with Additives to Improve Device Performance and Durability for Tin-Based Perovskite Solar Cells. *Energy Environ. Sci.* **2018**, *11*, 2353−2362.

(13) Jokar, E.; Chien, C. H.; Tsai, C. M.; Fathi, A.; Diau, E. W. -G. Robust Tin-Based Perovskite Solar Cells with Hybrid Organic Cations to Attain Efficiency Approaching 10%. *Adv. Mater.* **2019**, *31*, 1804835.

(14) Kamarudin, M. A.; Hirotani, D.; Wang, Z.; Hamada, K.; Nishimura, K.; Shen, Q.; Toyoda, T.; Iikubo, S.; Minemoto, T.; Yoshino, K.; Hayase, S. Suppression of Charge Carrier Recombination in Lead-Free Tin Halide Perovskite via Lewis Base Post-Treatment. *J. Phys. Chem. Lett.* **2019**, *10*, 5277−5283.

(15) Horn, J.; Scholz, M.; Oum, K.; Lenzer, T.; Schlettwein, D. Influence of Phenylethylammonium Iodide as Additive in the Formamidinium Tin Iodide Perovskite on Interfacial Characteristics and Charge Carrier Dynamics. *APL Mater.* **2019**, *7*, No. 031112.

(16) Liao, M.; Yu, B. B.; Jin, Z.; Chen, W.; Zhu, Y.; Zhang, X.; Yao, W.; Duan, T.; Djerdj, I.; He, Z. Efficient and Stable $FASnI_3$ Perovskite Solar Cells with Effective Interface Modulation by Low-Dimensional Perovskite Layer. *ChemSusChem* **2019**, *12*, 5007−5014.

(17) Li, M.; Zuo, W.-w.; Yang, Y.-G.; Aldamasy, M. H.; Wang, Q.; Cruz, S. H. T.; Feng, S.-L.; Saliba, M.; Wang, Z.-K.; Abate, A. Tin Halide Perovskite Films Made of Highly Oriented 2D Crystals Enable More Efficient and Stable Lead-Free Perovskite Solar Cells. *ACS Energy Lett.* **2020**, *5*, 1923.

(18) Jiang, X.; Wang, F.; Wei, Q.; Li, H.; Shang, Y.; Zhou, W.; Wang, C.; Cheng, P.; Chen, Q.; Chen, L.; Ning, Z. Ultra-High Open-Circuit Voltage of Tin Perovskite Solar Cells via an Electron Transporting Layer Design. *Nat. Commun.* **2020**, *11*, 1245.

(19) Nishimura, K.; Kamarudin, M. A.; Hirotani, D.; Hamada, K.; Shen, Q.; Iikubo, S.; Minemoto, T.; Yoshino, K.; Hayase, S. Lead-Free Tin-Halide Perovskite Solar Cells with 13% Efficiency. *Nano Energy* **2020**, *74*, 104858.

(20) Kamarudin, M. A.; Hirotani, D.; Wang, Z.; Hamada, K.; Nishimura, K.; Shen, Q.; Toyoda, T.; Iikubo, S.; Minemoto, T.; Yoshino, K.; Hayase, S. Suppression of Charge Carrier Recombination in Lead-Free Tin Halide Perovskite via Lewis Base Post-Treatment. *J. Phys. Chem. Lett.* **2019**, *10*, 5277−5283.

(21) Xu, P.; Chen, S.; Xiang, H.-J.; Gong, X.-G.; Wei, S.-H. Influence of Defects and Synthesis Conditions on the Photovoltaic Performance of Perovskite Semiconductor $CsSnI_3$. *Chem. Mater.* **2014**, *26*, 6068−6072.

(22) Yin, W.-J.; Shi, T.; Yan, Y. Unusual Defect Physics in $CH_3NH_3PbI_3$ Perovskite Solar Cell Absorber. *Appl. Phys. Lett.* **2014**, *104*, No. 063903.

(23) Long, R.; Liu, J.; Prezhdo, O. V. Unravelling the Effects of Grain Boundary and Chemical Doping on Electron−Hole Recombi-

nation in $CH_3NH_3PbI_3$ Perovskite by Time-Domain Atomistic Simulation. *J. Am. Chem. Soc.* **2016**, *138*, 3884−3890.
(24) Li, W.; Long, R.; Tang, J.; Prezhdo, O. V. Influence of Defects on Excited-State Dynamics in Lead Halide Perovskites: Time-Domain *Ab Initio* Studies. *J. Phys. Chem. Lett.* **2019**, *10*, 3788−3804.
(25) Pospisil, J.; Zmeskal, O.; Nespurek, S.; Krajcovic, J.; Weiter, M.; Kovalenko, A. Density of Bulk Trap States of Hybrid Lead Halide Perovskite Single Crystals: Temperature Modulated Space-Charge-Limited-Currents. *Sci. Rep.* **2019**, *9*, 3332.
(26) Kim, H.; Lee, Y. H.; Lyu, T.; Yoo, J. H.; Park, T.; Oh, J. H. Boosting the Performance and Stability of Quasi-Two-Dimensional Tin-Based Perovskite Solar Cells Using the Formamidinium Thiocyanate Additive. *J. Mater. Chem. A* **2018**, *6*, 18173−18182.
(27) Handa, T.; Aharen, T.; Wakamiya, A.; Kanemitsu, Y. Photoelectronic Properties of Lead-Free $CH_3NH_3SnI_3$ Perovskite Solar Cell Materials and Devices. In *Organic, Hybrid and Perovskite Photovoltaics XIX*; 2018; p 107371X.
(28) Handa, T.; Aharen, T.; Wakamiya, A.; Kanemitsu, Y. Radiative Recombination and Electron-Phonon Coupling in Lead-Free $CH_3NH_3SnI_3$ Perovskite Thin Films. *Phys. Rev. Mater.* **2018**, *2*, No. 075402.
(29) Monti, M.; Woolley, J. M.; Staniforth, M.; Wijesekara, A.; Tao, S. X.; Bandara, R. M. I.; Jayawardena, I.; Crocker, A.; Griffin, E.; Silva, S. R. P.; Hatton, R. A.; Lloyd-Hughes, J. Efficient Intraband Hot Carrier Relaxation in Sn and Pb Perovskite Semiconductors Mediated by Strong Electron-Phonon Coupling. *Proc. SPIE* **2019**, *10916*, 109160M.
(30) Kontos, A. G.; Kaltzoglou, A.; Arfanis, M. K.; McCall, K. M.; Stoumpos, C. C.; Wessels, B. W.; Falaras, P.; Kanatzidis, M. G. Dynamic Disorder, Band Gap Widening, and Persistent Near-IR Photoluminescence up to At Least 523 K in $ASnI_3$ Perovskites (A = $Cs^+$, $CH_3NH_3^+$ and $NH_2-CH{=}NH_2^+$). *J. Phys. Chem. C* **2018**, *122*, 26353−26361.
(31) Ma, L.; Hao, F.; Stoumpos, C. C.; Phelan, B. T.; Wasielewski, M. R.; Kanatzidis, M. G. Carrier Diffusion Lengths of over 500 nm in Lead-Free Perovskite $CH_3NH_3SnI_3$ Films. *J. Am. Chem. Soc.* **2016**, *138*, 14750−14755.
(32) Yang, Y.; Ostrowski, D. P.; France, R. M.; Zhu, K.; Van De Lagemaat, J.; Luther, J. M.; Beard, M. C. Observation of a Hot-Phonon Bottleneck in Lead-Iodide Perovskites. *Nat. Photonics* **2016**, *10*, 53−59.
(33) Manser, J. S.; Kamat, P. V. Band Filling with Free Charge Carriers in Organometal Halide Perovskites. *Nat. Photonics* **2014**, *8*, 737−743.
(34) Price, M. B.; Butkus, J.; Jellicoe, T. C.; Sadhanala, A.; Briane, A.; Halpert, J. E.; Broch, K.; Hodgkiss, J. M.; Friend, R. H.; Deschler, F. Hot-Carrier Cooling and Photoinduced Refractive Index Changes in Organic−Inorganic Lead Halide Perovskites. *Nat. Commun.* **2015**, *6*, 8420.
(35) Guo, Z.; Wan, Y.; Yang, M.; Snaider, J.; Zhu, K.; Huang, L. Long-Range Hot Carrier Transport in Hybrid Perovskites Visualized by Ultrafast Microscopy. *Science* **2017**, *356*, 59.
(36) Fu, J.; Xu, Q.; Han, G.; Wu, B.; Huan, C. H. A.; Leek, M. L.; Sum, T. C. Hot Carrier Cooling Mechanisms in Halide Perovskites. *Nat. Commun.* **2017**, *8*, 1300.
(37) Yuzawa, T.; Hamaguchi, H. Triplet Quantum Chain Process in the Photoisomerization of 9-Cis Retinal as Revealed by Nanosecond Time-Resolved Infrared Spectroscopy. *J. Mol. Struct.* **2010**, *976*, 414−418.
(38) Tanaka, S.; Kato, C.; Horie, K.; Hamaguchi, H. Time-Resolved Infrared Spectra and Structures of the Excited Singlet and Triplet States of Fluorenone. *Chem. Phys. Lett.* **2003**, *381*, 385−391.
(39) Jiang, X.; Hoffman, J.; Stoumpos, C. C.; Kanatzidis, M. G.; Harel, E. Transient Sub-Band-Gap States at Grain Boundaries of $CH_3NH_3PbI_3$ Perovskite Act as Fast Temperature Relaxation Centers. *ACS Energy Lett.* **2019**, *4*, 1741−1747.
(40) Park, J.-S.; Calbo, J.; Jung, Y.-K.; Whalley, L. D.; Walsh, A. Accumulation of Deep Traps at Grain Boundaries in Halide Perovskites. *ACS Energy Lett.* **2019**, *4*, 1321−1327.
(41) Shi, T.; Zhang, H.-S.; Meng, W.; Teng, Q.; Liu, M.; Yang, X.; Yan, Y.; Yip, H.-L.; Zhao, Y.-J. Effects of Organic Cations on the Defect Physics of Tin Halide Perovskites. *J. Mater. Chem. A* **2017**, *5*, 15124−15129.


https://dx.doi.org/10.1021/acs.jpclett.0c01589
*J. Phys. Chem. Lett.* 2020, 11, 5699−5704